Multifrequency Electrical Impedance Tomography Using Spectral Constraints

Emma Malone*, Gustavo Sato dos Santos, David Holder, and Simon Arridge

***Abstract*—Multifrequency electrical impedance tomography (MFEIT) exploits the dependence of tissue impedance on frequency to recover an image of conductivity. MFEIT could provide emergency diagnosis of pathologies such as acute stroke, brain injury and breast cancer. We present a method for performing MFEIT using spectral constraints. Boundary voltage data is employed directly to reconstruct the volume fraction distribution of component tissues using a nonlinear method. Given that the reconstructed parameter is frequency independent, this approach allows for the simultaneous use of all multifrequency data, thus reducing the degrees of freedom of the reconstruction problem. Furthermore, this method allows for the use of frequency difference data in a nonlinear reconstruction algorithm. Results from empirical phantom measurements suggest that our fraction reconstruction method points to a new direction for the development of multifrequency EIT algorithms in the case that the spectral constraints are known, and may provide a unifying framework for static EIT imaging.**

***Index Terms*—Electrical impedance tomography (EIT), image reconstruction–iterative, inverse methods.**

I. Introduction

MULTIFREQUENCY electrical impedance tomography (MEIT), or EIT spectroscopy (EITS), exploits the dependence of tissue impedance on frequency in order to recover an image of conductivity. A small current is injected and boundary voltage measurements are acquired using peripheral electrodes. Measurements are recorded simultaneously, or in rapid sequence, whilst varying the modulation frequency of the current. Data is compared to a reference frequency (frequency-difference) or considered independently (absolute imaging).

Time-difference EIT, which uses single-frequency measurements referred to a baseline, provides the gold-standard in EIT imaging, and the overwhelming majority of EIT clinical images have been produced using time-difference data. However, frequency-difference and absolute EIT could potentially allow for the imaging of an event without knowledge of a prior condition. This is necessary for diagnostic imaging of conditions such as acute stroke, brain injury, and breast cancer, because patients are admitted into care after the onset of the pathology and a baseline recording of healthy tissue is not available [1]–[3].

The challenge of multifrequency EIT lies in the high sensitivity of the solution to modelling and instrumentation errors [4], [5]. Simple frequency-difference methods, which attempt to reconstruct an image from data referred to a low frequency using a linear method, have proved effective in the case of resolving a frequency dependent anomaly from a homogeneous, frequency invariant background [6]. The weighted frequency difference algorithm, which uses a weighted difference between data acquired at two frequencies and a linear method, has been shown to successfully enhance the contrast given by an anomaly in a frequency dependent background [7]–[9].

Preliminary studies suggest that nonlinear reconstruction methods using absolute data hold the potential for clinical imaging [10], [11]. However, absolute imaging fails to suppress artefacts caused by the high sensitivity of EIT to modelling errors.

Whereas multifrequency EIT is at an early stage of development, an extensive literature has been produced on the related subject of multispectral diffuse optical tomography (DOT). In particular, DOT research has produced methods for directly reconstructing chromophore concentrations using the wavelength dependence of tissue properties [12].

In this paper, a method is introduced for using frequency-difference data in a nonlinear reconstruction scheme by use of spectral constraints. We propose to use all multifrequency data directly to reconstruct the volume fraction distribution of the tissues. The results of numerical validation and application of our method to phantom experimental data recorded with the UCLH Mark 2.5 MFEIT system [13] are presented. The robustness of our direct multifrequency method is discussed and compared to an indirect method for estimating the fractions from the absolute conductivity images. The question of how fraction imaging compares to weighted frequency-difference imaging in tank experiments is addressed. The performance of fraction imaging is compared with weighted frequency-difference on simulated data that violates the assumptions of the latter method. Finally, the approximation introduced by our fraction model is investigated and discussed.

A. Forward Problem

The forward problem consists in determining the potential $\boldsymbol{u}$ from knowledge of the conductivity distribution $\boldsymbol{\sigma}$ and the Neumann boundary conditions. The forward map $A : \boldsymbol{\sigma} \rightarrow \boldsymbol{v}$ relates the conductivity distribution to boundary voltage measurements

Manuscript received July 29, 2013; accepted September 24, 2013. Date of publication October 09, 2013; date of current version January 30, 2014. *Asterisk indicates corresponding author.*

*E. Malone is with the Department of Medical Physics and Bioengineering, University College London, WC1E 6BT London, U.K. (e-mail: emma.malone.11@ucl.ac.uk).

G. S. dos Santos and D. Holder are with the Department of Medical Physics and Bioengineering, University College London, WC1E 6BT London, U.K.

S. Arridge is with the Department of Computer Science, University College London, WC1E 6BT London, U.K.

Color versions of one or more of the figures in this paper are available online at http://ieeexplore.ieee.org.

Digital Object Identifier 10.1109/TMI.2013.2284966

$\boldsymbol{v}$ for an assumed physical model. An analytical solution to the forward problem can be obtained only in the case of simple geometries, otherwise it is necessary to pursue numerical methods such as the finite element method (FEM).

B. Inverse Problem

The inverse problem consists in estimating the internal conductivity distribution of an object for which the Neumann-to-Dirichlet map is known. Nonlinear methods for reconstructing an EIT image $\boldsymbol{\sigma}$ from boundary voltage data $\boldsymbol{v}$ involve the iterative minimization of an objective function of the form

$$l\left(A(\boldsymbol{\sigma}), \boldsymbol{v}\right) + \tau \Psi\left(\boldsymbol{\sigma}\right) \tag{1}$$

where l is the negative log-likelihood, Ψ is a regularizing function, and τ is the regularization parameter.

II. Method

A. Fraction Model

The fraction model is a representation of the conductivity of an object. We employ the fraction model in conjunction with the FEM to approximate a conductivity distribution. It is assumed that the object is composed of a limited number of tissues and that a volume fraction, or concentration value, can be determined for each component and element of the mesh. The spatial distribution of the tissues is then described by the corresponding fraction distributions. Furthermore, the assumption that the tissues are homogeneous and have characteristic spectral properties allows for the expression of the conductivity of the object in terms of the conductivity of individual components.

Let us consider a 3-D domain on which a frequency dependent conductivity distribution $\boldsymbol{\sigma}(\boldsymbol{x}, \omega)$ is defined, where $\boldsymbol{x}$ denotes the spatial coordinates, and ω the frequency. The conductivity is assumed to be static. A discretization of the domain is performed, and the conductivity is approximated using the FEM to represent an element based, piecewise constant distribution. As a result, the conductivity can be represented by the mesh and a frequency dependent, $N \times 1$ vector that determines the value of each element $\boldsymbol{\sigma} = [\sigma_n(\omega);\ n = 1, \ldots, N]$, where N is the number of elements. Time-harmonic currents are injected at the boundary at M frequencies $\omega_1, \ldots, \omega_i, \ldots, \omega_M$ and K real boundary voltage measurements $\boldsymbol{v} = [v_k(\omega);\ k = 1, \ldots, K]$ are acquired for each frequency.

The following assumptions are made.

1) The domain is composed of a known number T of tissues $t_1, \ldots, t_j, \ldots, t_T$ with distinct conductivity.
2) The conductivity of each tissue is known for all measurement frequencies $\epsilon_{ij} = \sigma^{t_j}(\omega_i)$.
3) The conductivity of the nth element is given by the linear combination of the conductivities of the component tissues

$$\sigma_n(\omega_i) = \sum_{j=1}^{T} f_{nj} \cdot \epsilon_{ij} \tag{2}$$

where $0 \leq f_{nj} \leq 1$ and $\sum_{j=1}^{T} f_{nj} = 1$.

Each weighting value f_{nj} of the linear combination is the volume fraction, or concentration, of the jth tissue in the nth voxel. If the nth voxel is occupied only by the jth tissue, then the conductivity is that of the tissue $\sigma(\omega_i) = \epsilon_{ij}$. In this case $f_{nj} = 1$ and $f_{nl} = 0\ \forall l \neq j$. In the case that the voxel lies along a tissue boundary, or is otherwise occupied by a mixture of tissues, the conductivity is approximated by the linear combination of the conductivities of the components, weighted by their fraction values.

Under these assumptions the relationship between conductivity and boundary voltages can be rewritten in terms of the matrix $\mathbf{F} = \left\{\boldsymbol{f}_1, \ldots, \boldsymbol{f}_j, \ldots, \boldsymbol{f}_T\right\}$, of dimensions $N \times T$. The fraction values are independent of frequency and constant across all measurements. Using the chain rule we obtain, for $j = 1, \ldots, T$

$$\frac{\partial A(\boldsymbol{\sigma}_i)}{\partial \boldsymbol{f}_j} = \frac{\partial A(\boldsymbol{\sigma}_i)}{\partial \boldsymbol{\sigma}_i} \frac{\partial \boldsymbol{\sigma}_i}{\partial \boldsymbol{f}_j} = \frac{\partial A(\boldsymbol{\sigma}_i)}{\partial \boldsymbol{\sigma}_i} \epsilon_{ij} = \mathbf{J}(\boldsymbol{\sigma}_i) \cdot \epsilon_{ij} \tag{3}$$

where $\boldsymbol{\sigma}_i = \boldsymbol{\sigma}(\omega_i)$ and $\mathbf{J}(\boldsymbol{\sigma}_i)$ is the Jacobian of the forward map at the frequency ω_i.

B. Fraction Image Reconstruction

Assuming the noise is white Gaussian, the objective function for conductivity imaging (1) becomes

$$\boldsymbol{\sigma}_i = \arg\min_{\boldsymbol{\sigma}_i} \frac{1}{2} \left[\left\| A(\boldsymbol{\sigma}_i) - \boldsymbol{v}(\omega_i) \right\|^2 + \tau \Psi\left(\boldsymbol{\sigma}_i\right) \right] \tag{4}$$

for each frequency ω_i.

In analogy with conductivity imaging, we attempt to reconstruct the fraction distributions of all tissues by minimizing a regularized objective function of the form

$$\frac{1}{2} \left[\left\| A\left(\sum_{j=1}^{T} \boldsymbol{f}_j \epsilon_{ij} \right) - \boldsymbol{v}(\omega_i) \right\|^2 + \tau \Psi(\mathbf{F}) \right]. \tag{5}$$

Using relative data, referred to a chosen frequency ω_0, the residual error becomes

$$\frac{1}{2} \left\| \frac{A\left(\sum_j \boldsymbol{f}_j \epsilon_{ij}\right) - A\left(\sum_j \boldsymbol{f}_j \epsilon_{0j}\right)}{A\left(\sum_j \boldsymbol{f}_j \epsilon_{0j}\right)} - \frac{\boldsymbol{v}(\omega_i) - \boldsymbol{v}(\omega_0)}{\boldsymbol{v}(\omega_0)} \right\|^2. \tag{6}$$

We use a Markov random field (MRF) regularization term of the form

$$\frac{1}{2} \sum_{j=1}^{T} \sum_{n=1}^{N} \sum_{l(n)} |f_{nj} - f_{l(n)j}|^2 \tag{7}$$

where $l(n)$ runs over all neighbors of the nth voxel.

Finally, if all multifrequency measurements are considered simultaneously, we obtain

$$\Phi(\mathbf{F}) = \frac{1}{2} \left[\sum_{i=1}^{M} \left\| \frac{A\left(\sum_j \boldsymbol{f}_j \epsilon_{ij}\right) - A\left(\sum_j \boldsymbol{f}_j \epsilon_{0j}\right)}{A\left(\sum_j \boldsymbol{f}_j \epsilon_{0j}\right)} - \frac{\boldsymbol{v}(\omega_i) - \boldsymbol{v}(\omega_0)}{\boldsymbol{v}(\omega_0)} \right\|^2 + \tau \sum_{j=1}^{T} \sum_{n=1}^{N} \sum_{l(n)} |f_{nj} - f_{l(n)j}|^2 \right]. \tag{8}$$

The objective function $\Phi(\mathbf{F})$ is differentiable and the gradient is obtained via the chain rule (3).

Fraction reconstruction algorithm outline

Initialize $t = 0$, $\boldsymbol{f}_1 = \mathbf{1}$ for the background tissue, and $[\boldsymbol{f}_2, \ldots, \boldsymbol{f}_T] = \mathbf{0}$ for all other tissues
set tol and $maxit$
repeat
  find Cauchy point $\tilde{\mathbf{F}}$ using gradient projection
  solve (10) to find $\boldsymbol{d}^t$
  find β_t that minimizes $\Phi(\tilde{\boldsymbol{f}}_j + \beta^t \boldsymbol{d}_j^t;\ j = 2, \ldots, T)$
  compute $\mathbf{F}^+$ using (11)
  set $\mathbf{F}^{t+1}$ using (12)
  $t = t + 1$
until $\left|\Phi(\mathbf{F}^{t+1}) - \Phi(\mathbf{F}^t)\right| \leq tol$ or $t = maxit$
return $\mathbf{F}$

Algorithm 1. Schematic comparison between direct and indirect fraction reconstruction methods.

The constraint $\sum_{j=1}^{T} f_{nj} = 1\ \forall n$ is enforced by substituting $\boldsymbol{f}_1 = \mathbf{1} - \sum_{j=2}^{T} \boldsymbol{f}_j$ in the objective function. The $T-1$ fraction images, are reconstructed using

$$[\boldsymbol{f}_2, \ldots, \boldsymbol{f}_T] = \arg \min_{\boldsymbol{f}_2, \ldots, \boldsymbol{f}_T} \Phi\left(\mathbf{1} - \sum_{j=2}^{T} \boldsymbol{f}_j, \boldsymbol{f}_2, \ldots, \boldsymbol{f}_T\right) \tag{9}$$

where $0 \leq f_{nj} \leq 1$, and remaining fraction is simply $\boldsymbol{f}_1 = \mathbf{1} - \sum_{j=2}^{T} \boldsymbol{f}_j$.

The reconstruction of $[\boldsymbol{f}_2, \ldots, \boldsymbol{f}_T]$ was constrained to the closed interval $[\mathbf{0},\ \mathbf{1}]$ and performed using a two-step algorithm.

1) Step 1: Gradient Projection: Gradient projection is a method for optimizing an objective function with bounded variables [14]. Initially the minimization is set to follow the negative gradient direction, but the search path is projected onto the constraint whenever an upper or lower constraint is encountered. The corners of the search path are found by computing the step size values for which each variable reaches a constraint. The objective function is approximated by the quadratic form along each straight section of the search path, and the minimum of the objective function is found by differentiating with respect to the step size. Each section is considered in sequence until a solution that satisfies the constraints is found. The result of the gradient projection step is the Cauchy point $\tilde{\mathbf{F}} = \left[\tilde{\boldsymbol{f}}_1, \tilde{\boldsymbol{f}}_2, \ldots, \tilde{\boldsymbol{f}}_T\right]$, satisfying $\sum_{j=1}^{T} \tilde{\boldsymbol{f}}_j = \mathbf{1}$.

2) Step 2: Damped Gauss–Newton Using a Krylov Solver: The components of the Cauchy point that coincide with the constraints define the active sets for the second step. These are fixed to the constraint value and the subproblem of solving for all other components is considered. Initially the constraints are ignored, one step of a damped Gauss–Newton method is performed and then the solution is projected back onto the constraints.

The search direction $\boldsymbol{d}^t$ at iteration t is calculated by solving

$$\mathbf{H}(\tilde{\boldsymbol{f}}_2, \ldots, \tilde{\boldsymbol{f}}_T) \cdot \boldsymbol{d}^t = -\nabla\Phi(\tilde{\boldsymbol{f}}_2, \ldots, \tilde{\boldsymbol{f}}_T) \tag{10}$$

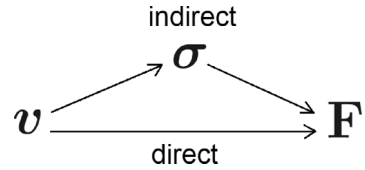

Fig. 1. Schematic comparison between direct and indirect fraction reconstruction methods.

for the components with nonactive sets. The Hessian matrix $\mathbf{H}$ is approximated using the Gauss–Newton form by disregarding the second order derivative of the residual error. Given the size of the problem, the approximated Hessian is never formulated explicitly and (10) is solved using generalized minimal residuals (GMRes) [15]. The minimization step size β^t is computed using the Brent line-search method [16], and the Brent abscissae are found via a gold-section bracketing loop [17]. The result of the damped Gauss–Newton step is

$$\mathbf{F}^+ = \begin{cases} \mathbf{1} - \sum_{j=2}^{T} (\tilde{\boldsymbol{f}}_j + \beta^t \cdot \boldsymbol{d}_j^t) & j = 1 \\ \tilde{\boldsymbol{f}}_j + \beta^t \cdot \boldsymbol{d}_j^t & 2 \leq j \leq T \end{cases} \tag{11}$$

and the proposed solution is given by

$$\boldsymbol{f}_{ni}^{t+1} = \begin{cases} 0, & \text{if } \tilde{\boldsymbol{f}}_{ni} = 0 \text{ or } \boldsymbol{f}_{ni}^+ \leq 0 \\ 1, & \text{if } \boldsymbol{f}_{ni} = 1 \text{ or } \boldsymbol{f}_{ni}^+ \geq 1 \\ \boldsymbol{f}_{ni}^+, & \text{otherwise.} \end{cases} \tag{12}$$

The solution is accepted if $\Phi(\mathbf{F}^{t+1}) \leq \Phi(\tilde{\mathbf{F}}) \leq \Phi(\mathbf{F}^t)$. If only $\Phi(\tilde{\mathbf{F}}) \leq \Phi(\mathbf{F}^t)$ then the Cauchy point is accepted.

C. Fraction Image Reconstruction: Indirect Method

An alternative method for estimating the tissue fractions indirectly is by fitting the absolute conductivity images (Fig. 1). First, the conductivity images at each frequency $\{\boldsymbol{\sigma}_i;\ i = 1, \ldots, M\}$ are obtained by minimizing (4)

$$\boldsymbol{\sigma}_i = \arg \min_{\boldsymbol{\sigma}_i} \frac{1}{2} \left[\|A(\boldsymbol{\sigma}_i) - \boldsymbol{v}_i\|^2 + \tau_i \sum_{n=1}^{N} \sum_{l(n)} |\sigma_{ni} - \sigma_{l(n)i}|^2 \right] \tag{13}$$

using a nonlinear Gauss–Newton–Krylov algorithm [18]. The regularization parameters τ_i are optimized for each frequency. Then, the indirect fraction image $\hat{\mathbf{F}} = \left[1 - \sum_{j=2}^{T} \hat{\boldsymbol{f}}_j, \hat{\boldsymbol{f}}_2, \ldots, \hat{\boldsymbol{f}}_T\right]$ is computed by minimizing

$$\frac{1}{2} \left[\sum_{i=1}^{M} \left\| \boldsymbol{\sigma}_i - \left(\mathbf{1} \cdot \epsilon_{i1} + \sum_{j=2}^{T} \hat{\boldsymbol{f}}_j \cdot (\epsilon_{ij} - \epsilon_{i1}) \right) \right\|^2 + \right. \\ \left. + \ \xi \sum_{j=1}^{T} \sum_{n=1}^{N} \sum_{l(n)} |\hat{f}_{nj} - \hat{f}_{l(n)j}|^2 \right] \tag{14}$$

where ξ is the regularization parameter. The minimization is performed, as for the proposed direct method, by alternating steps of gradient projection and damped Gauss–Newton.

D. Image Quantification

In evaluating experimental results, image quality was assessed on the basis of an objective quantification method. We considered the case of resolving a perturbation of tissue t_2 from a homogeneous background of tissue t_1 by reconstructing an image of the fraction $\boldsymbol{f}_2$. The reconstructed perturbation was identified as the largest connected cluster of voxels with values larger than 50% of the maximum displacement from the mean value of the image [6], [19]. We devised three measures of image quality.

1) Image noise: inverse of the contrast-to-noise ratio (CNR) between the real perturbation Σ and the background

$$\frac{\sqrt{\frac{1}{N^B-1}\sum_{n\notin\Sigma}\left(f_{n2}-\bar{f}_2^B\right)^2}}{\left|\bar{f}_2^P-\bar{f}_2^B\right|} \tag{15}$$

where $\bar{f}_2^P$ and $\bar{f}_2^B$ are the mean intensities of the real perturbation and background, and N^B is number of elements of the background.

2) Localization error: ratio between the norm of the x-y displacement of the center of mass of the reconstructed perturbation Σ' from the real position (x, y), and the diameter of the mesh d

$$\frac{\left\|\sum_{n\in\Sigma'} f_{n2}\cdot(x_n,y_n)-(x,y)\right\|}{d} \tag{16}$$

where (x_n, y_n) is the x-y position of the center of the nth tetrahedron.

3) Shape error: mean ratio of the difference between the dimensions of the real and reconstructed perturbations, respectively (l_x, l_y, l_z) and (l'_x, l'_y, l'_z), and the diameter of the mesh

$$\frac{1}{3}\left(\frac{|l_x-l'_x|+|l_y-l'_y|}{d}+\frac{|l_z-l'_z|}{h}\right) \tag{17}$$

where h is the height of the mesh. The real dimensions of the perturbation were measured with a calliper, and the size of the reconstructed perturbation was estimated by taking the maximum coordinate difference between elements coinciding with the perturbation.

III. Results and Discussion

A. Tissue Impedance Spectra

The spectral values of the test tissues were obtained empirically from tissue samples. Resistance measurements were acquired with a Hewlett-Packard 42847A (Hewlett-Packard, Palo Alto, CA, USA) impedance analyzer for 48 frequencies in the range 20 Hz–1 MHz using Ag-AgCl electrodes.

We used biological test objects with frequency dependent conductivities to mimic the properties of live tissues [6], [8], [9]. The background medium was a mixture of 0.1% concentration NaCl solution and carrot cubes of approximately 4 mm per side. Two samples were measured using Perspex tubes of fixed diameter (1.6 cm) and variable length (4.6 and 7.5 cm).

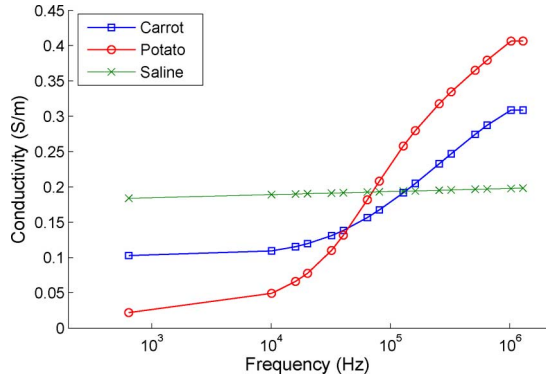

Fig. 2. Conductivity values of test tissues obtained from sample measurements at 16 output frequencies of the UCLH Mk 2.5 multifrequency EIT system in the range 640 Hz–1.29 MHz.

A perturbation was obtained from a potato segment of diameter approximately 4.6 cm. The resistivities of the full length (10.6 cm) and partial length (5.4 cm) were measured. The test object was immersed in saline for 45 min before starting the recordings in order to reduce drift. The electrode resistance was estimated and subtracted by plotting resistance against length for each tissue and evaluating the offset of the line passing through the measurement points. The conductivities of the carrot-saline background and potato perturbation rose monotonically from 0.1 S/m and 0.02 S/m at 20 Hz to 0.3 S/m and 0.4 S/m at 1 MHz.

These results were used to simulate realistic data and to reconstruct fraction images from experimental EIT recordings made with the UCLH Mk. 2.5 system. The conductivity values for 16 amongst the output frequencies of the UCLH system in the range 640 Hz–1.29 M Hz were estimated from the spline of the sample measurements (Fig. 2).

B. Numerical Validation

Numerical validation of the proposed fraction reconstruction method was performed on synthetic data. Boundary voltages were simulated using a cylindrical mesh of diameter 19 cm and height 10 cm, with 62 784 elements and a ring of 32 electrodes around the center. A current of peak amplitude 133 μA, injected through polar electrodes, was simulated. For each injection pair we considered the difference between voltages on all adjacent pairs of electrodes not involved in delivering the current, for a total of 448 measurements per frequency. The ground point was fixed at the center of the bottom of the mesh. The complete electrode model [20] was employed, and the electrode impedance was set to 1 kΩ.

A cylindrical perturbation of diameter 4.6 cm and height 10 cm was placed in (-4 cm 0 cm 0 cm) (position 1) and (0 cm $+4$ cm 0 cm) (position 2), where the origin is the center of the tank. The background and perturbation conductivities were set to the values for saline-carrot and potato obtained empirically for 16 output frequencies of the UCLH Mk 2.5 system. All measurements were referred to the lowest frequency of 640 Hz. Proportional 0.1% white Gaussian noise was added to the absolute boundary voltages. The noise level was chosen under consideration that the expected change across frequencies in boundary voltages is in the order of 1%, therefore a high level of precision must be achieved in measuring the absolute values with an EIT system. The regularization parameter was set using the L-curve

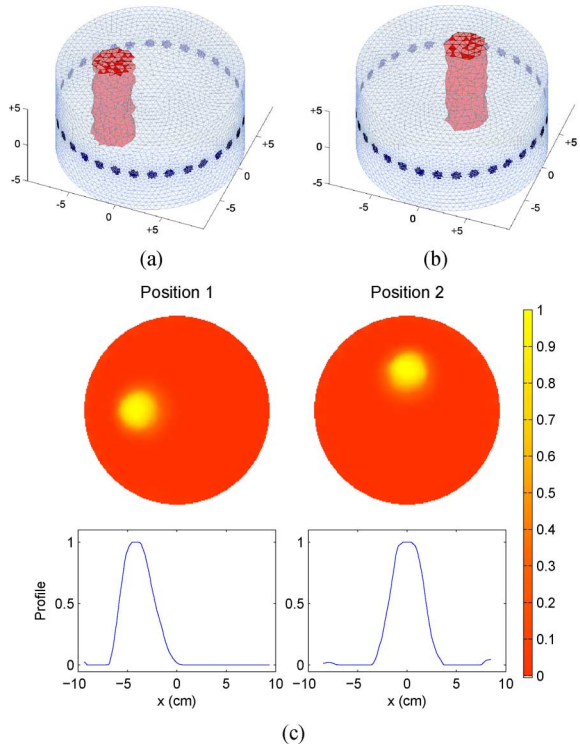

Fig. 3. Numerical validation model and results: (a) model of position 1 (-4 cm 0 cm 0 cm), (b) model of position 2 (0 cm $+4$ cm 0 cm), (c) perturbation fraction images of positions 1 and 2. In all images we display the raster of the central slice ($z = 0$, thickness 2 cm) and, where relevant, profile plots at $y = 0$ cm for position 1 and $y = +4$ cm for position 2. The scale is the volume fraction value.

method [21]. Fraction images were reconstructed using all multifrequency data by performing four iterations of the proposed nonlinear fraction reconstruction method (Fig. 3).

C. Robustness to Spectral Errors

The fraction model assumes exact knowledge of the impedance spectra of all tissues in the domain. These values were evaluated by measuring the conductivity of tissue samples with an impedance analyzer, as described in Section III-A. It is inevitable that these measurements are affected by noise and experimental error, and the tissue spectra employed in the reconstruction scheme are incorrect. We performed a simulation study to determine the robustness of our fraction reconstruction method to errors in the assumed tissue spectra $\boldsymbol{\epsilon}_j = \{\epsilon_{ij};\ i = 1, \ldots, M\}$. The same mesh, electrodes, measurement protocol, and perturbation were chosen as in the previous section. A random error was added to the tissue spectra of carrot ($\boldsymbol{\epsilon}_1$) and potato ($\boldsymbol{\epsilon}_2$), before producing a conductivity model

$$\sigma^*_{ni} = \begin{cases} \epsilon_{i1} + \mathrm{Rand}(\epsilon_{i1}, \epsilon_{i1} \cdot \Sigma), & \text{on the background} \\ \epsilon_{i2} + \mathrm{Rand}(\epsilon_{i2}, \epsilon_{i2} \cdot \Sigma), & \text{on the perturbation} \end{cases} \tag{18}$$

where $\mathrm{Rand}(\epsilon_{ij}, \epsilon_{ij} \cdot \Sigma)$ is a random number drawn from the normal distribution with mean ϵ_{ij} and variance $\epsilon_{ij} \cdot \Sigma$. In an experimental setup, the values $\epsilon_{ij} + \mathrm{Rand}(\epsilon_{ij}, \epsilon_{ij} \cdot \Sigma)$ are the real, unknown, conductivities of the tissues, whereas the mean conductivities ϵ_{ij} are the inexact measurements obtained from the samples.

TABLE I
ROBUSTNESS TO SPECTRAL ERRORS: MEAN AND STANDARD DEVIATION OVER 20 REPETITIONS OF IMAGE ERROR Err_{L^2} FOR SEVERAL CHOICES OF SPECTRAL VARIANCE Σ

Σ	1%	3%	5%	10%
$mean(\mathrm{Err}_{L^2})$	1.17%	1.88%	2.87%	3.09%
$var(\mathrm{Err}_{L^2})$	$4.4 \cdot 10^{-6}$	$7.2 \cdot 10^{-5}$	$2.6 \cdot 10^{-4}$	$2.3 \cdot 10^{-4}$

Boundary voltage data was simulated using the model $\boldsymbol{\sigma}^*$, and fraction images were reconstructed using the inexact measured spectra. The process was repeated 20 times for each choice of $\Sigma = \{1\%, 3\%, 5\%, 10\%\}$. The regularization parameter was $\tau = 10^{-3}$, and the number of iterations was 4 in all cases.

The results were evaluated by computing the ratio of the L^2-norm of the distance between the reconstructed image and the true solution, and the L^2-norm of the true solution. To make the error measure independent of the number of tissues, the mean was taken

$$\mathrm{Err}_{L^2} = \frac{1}{T} \sum_{j=1}^{T} \frac{\left\| \boldsymbol{f}_j^{\mathrm{recon}} - \boldsymbol{f}_j^{\mathrm{true}} \right\|}{\left\| \boldsymbol{f}_j^{\mathrm{true}} \right\|} \tag{19}$$

where

$$\boldsymbol{f}_2^{\mathrm{true}} = \begin{cases} 0, & \text{on the background} \\ 1, & \text{on the perturbation} \end{cases} \tag{20}$$

and $\boldsymbol{f}_1^{\mathrm{true}} = \mathbf{1} - \boldsymbol{f}_2^{\mathrm{true}}$. The mean and standard deviation of the error over 20 repetitions was computed for each choice of Σ (Table I).

We computed the mean and the standard deviation of the reconstructed images [Fig. 4(a) and (b)], and the mean image quantification measures [Fig. 4(c)]. We observed that for $\Sigma = 1\%$ the images were similar to the result obtained using the exact spectra (Fig. 3). We note that in the latter case, in which the same spectra are used to generate the data and reconstruct the image, $\mathrm{Err}_{L^2} = 1.06\%$. For $\Sigma = 3\%$ and $\Sigma = 5\%$ the shape and position of the perturbation were generally reconstructed with sufficient accuracy, but a reduction in contrast was observed in most images. For $\Sigma = 10\%$ the image quality was affected, and in some cases the perturbation could not be identified. The mean relative contrast between the tissues is

$$C^{\%} = \frac{1}{M} \sum_{i=1}^{M} \frac{(\epsilon_{i2} - \epsilon_{i1})}{\epsilon_{i1}} \approx 34\% \tag{21}$$

therefore it is reasonable to expect that a 10% error on the spectra would make it difficult to distinguish between the tissues.

D. Phantom Study

A phantom study was designed to reproduce the experimental setup rendered previously in simulation. The phantom was built using the test tissues measured with the impedance analyzer, and a perspex cylindrical tank of diameter 19 cm and height 10 cm. The potato was placed in (-4 cm 0 cm 0 cm) [Fig. 5(a)] and (0 cm $+4$ cm 0 cm) [Fig. 5(b)] and immersed in the saline-

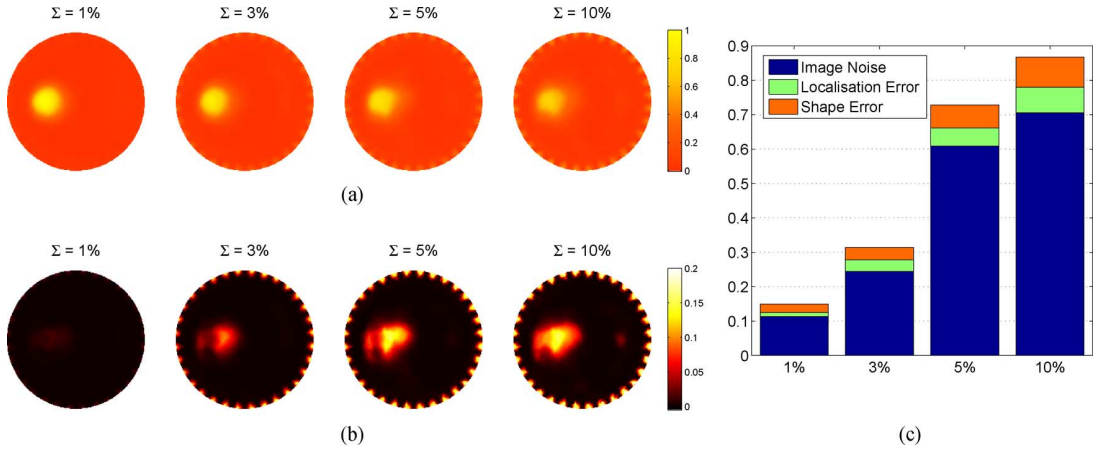

Fig. 4. Robustness to spectral errors results: (a) mean and (b) standard deviation of the reconstructed fraction images for each choice of the spectral variance Σ; (c) mean image quantification results over 20 repetitions for each choice of Σ.

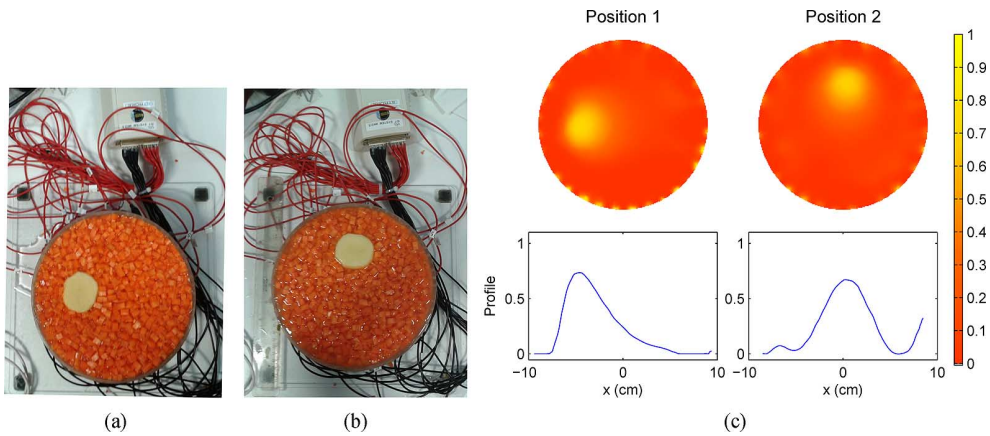

Fig. 5. Phantom experiment setup and fraction images: (a) position 1 (−4 cm 0 cm 0 cm), (b) position 2 (0 cm +4 cm 0 cm), (c) perturbation fraction images of positions 1 and 2.

carrot mixture. A ring of 32 silver electrodes with 1 cm diameter was placed around the tank and a 33rd electrode was used to fix the ground at the center of the base. Measurements were recorded using the UCLH Mark 2.5 MFEIT system at 16 frequencies in the range 640 Hz–1.29 MHz. A current of amplitude 133μA was injected at polar electrode pairs and voltages were acquired at all adjacent channels not involved in the current injection. The data was averaged over 10 frames and referred to the lowest frequency (640 Hz). Images were reconstructed using the same mesh employed in validating the method. In the following, unless otherwise specified, the regularization parameter was selected using the L-curve method, and the number of iterations for nonlinear methods was set to 4. The electrode contact impedance was assumed to be 1 kΩ, which is the upper limit of the real value, and constant across all electrodes and frequencies.

Fraction images were reconstructed using the proposed method from all multifrequency data [Fig. 5(c)].

E. Comparison With Indirect Fraction Estimation

Fraction images were obtained from the multifrequency phantom data using the indirect method described previously. Absolute conductivity values were recovered for each measurement frequency [Fig. 6(a) and (b)] and fraction images were obtained from these [Fig. 6(c)]. The conductivity images present an area of high conductivity area around the edge of the tank, which is caused by inaccurate modelling of the boundary geometry, electrode placement, shape, and size, and contact impedance. In the fraction images this artefact is reduced because frequency invariant errors are subtracted from the data. The conductivity images obtained in the frequency range 30–80 kHz present very low contrast. This is in agreement with the tissue sample conductivity measurements in that the spectra of potato and carrot-saline are very similar in the same frequency range. It is evident by visual comparison that the use of spectral constraints can result in a significant improvement in image quality, when compared to absolute conductivity imaging.

The fraction images obtained with the direct fraction reconstruction method were compared with the images obtained using the indirect method, and the absolute conductivity images [Fig. 6(d) and (e)]. The results suggest that the proposed fraction reconstruction method is more robust than absolute conductivity imaging and the indirect method. The proposed fraction reconstruction algorithm employs the boundary voltage data directly, and a single optimization problem is solved. To image the fractions from the absolute conductivity, first an optimization problem is solved for each frequency to reconstruct the conductivity images, then the fitting parameters are computed. The direct reconstruction algorithm uses all multifrequency data to estimate the regularization prior, whereas the indirect method requires that the regularization is first

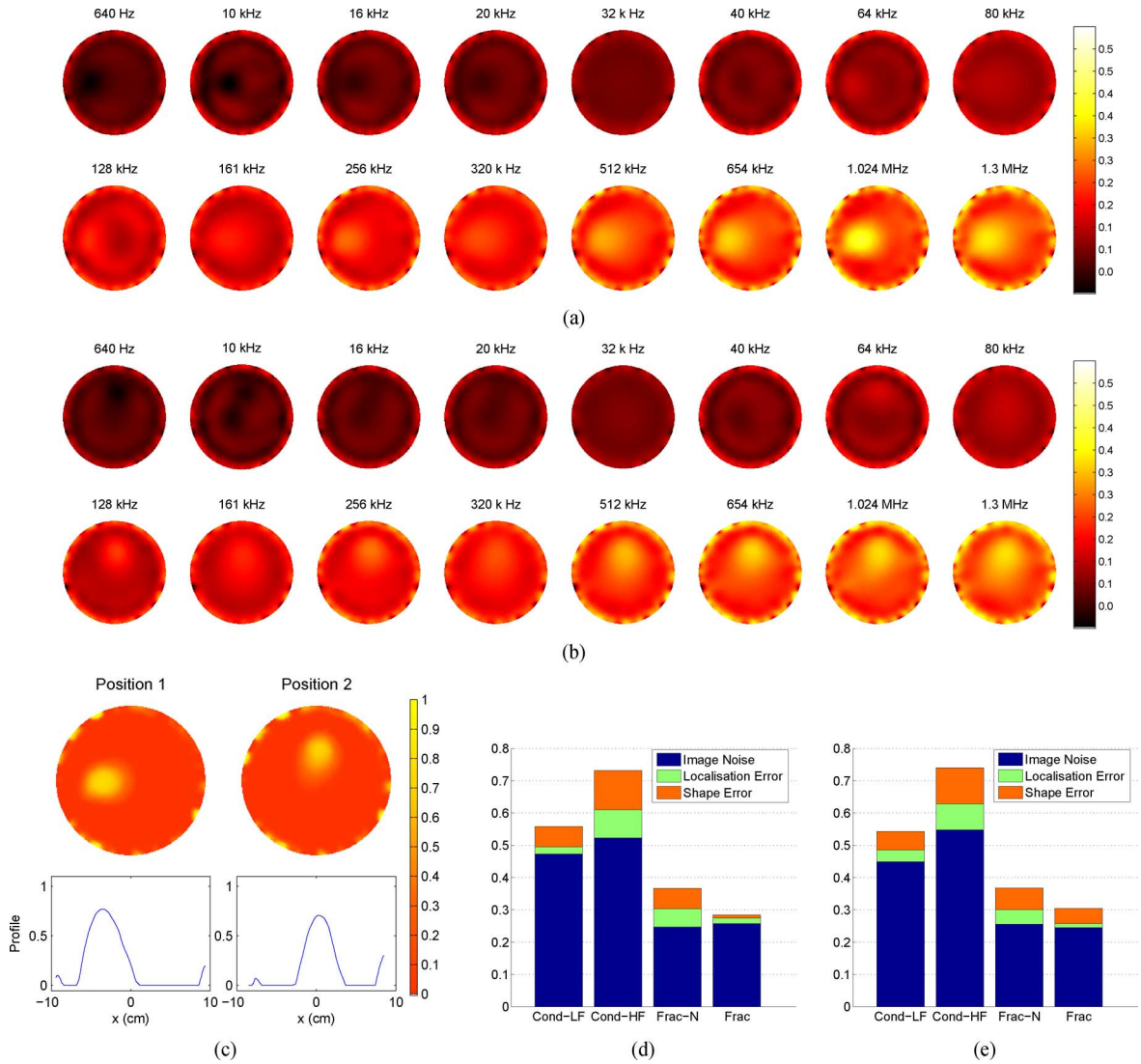

Fig. 6. Phantom absolute conductivity images for each measurement frequency: (a) position 1 and (b) position 2. The scale is *S/m*. Multifrequency imaging results: (c) fractions obtained using indirect method for positions 1 and 2. Comparison of image quantification results for absolute conductivity images at 640 Hz (Cond-LF) and 1.2 MHz (Cond-HF), and fraction images from indirect method (Frac-I) and direct method (Frac): (d) position 1, (e) position 2.

optimized independently for each frequency and then again for computing the fractions.

F. Comparison With Weighted Frequency-Difference Conductivity Imaging

The weighted frequency-difference (WFD) algorithm uses a weighted difference in boundary voltages between two frequencies $\boldsymbol{v}_i - \delta_i \boldsymbol{v}_0$ and a linear method to reconstruct a weighted conductivity difference $\boldsymbol{\sigma}_0 - \delta_i \boldsymbol{\sigma}_i$, where $\delta_i = \langle \boldsymbol{v}(\omega_i), \boldsymbol{v}(\omega_0) \rangle / \langle \boldsymbol{v}(\omega_0), \boldsymbol{v}(\omega_0) \rangle$. WFD conductivity images were reconstructed from the tank data for each frequency and compared to fraction images [Fig. 7(a) and (b)]. The lowest frequency ($\omega_0 = 640$ Hz) was used as a reference and the reconstruction was performed using generalized tSVD and MRF regularization [22]. The image quantification results [Fig. 7(c) and (d)] are comparable to fraction imaging in this case.

G. Spectral Constraints Method for Nonlinear Case

Application of the weighted frequency-difference algorithm is limited by the following assumptions:

1) $\boldsymbol{\sigma}_0 - \delta_i \boldsymbol{\sigma}_i \approx 0$ on a large background area and on the boundary;
2) $\boldsymbol{\sigma}_0 - \delta_i \boldsymbol{\sigma}_i \neq 0$ on a small anomaly.

Furthermore, use of a linear reconstruction scheme requires the added assumption that linear changes in conductivity result in linear changes in boundary voltages. In the case of the phantom experiment these assumptions are valid because the object consists in a small, low-contrast perturbation immersed in a large homogeneous background.

In order to investigate further application of WFD and our fraction method we simulated two conductivity distributions that violate the assumptions of WFD [Fig. 8(a) and (b)]. As previously, the measured spectral values of the saline-carrot and potato samples were used to simulate boundary voltage measurements, and 0.1% white Gaussian noise was added the data. The lowest frequency (640 Hz) was used as a reference.

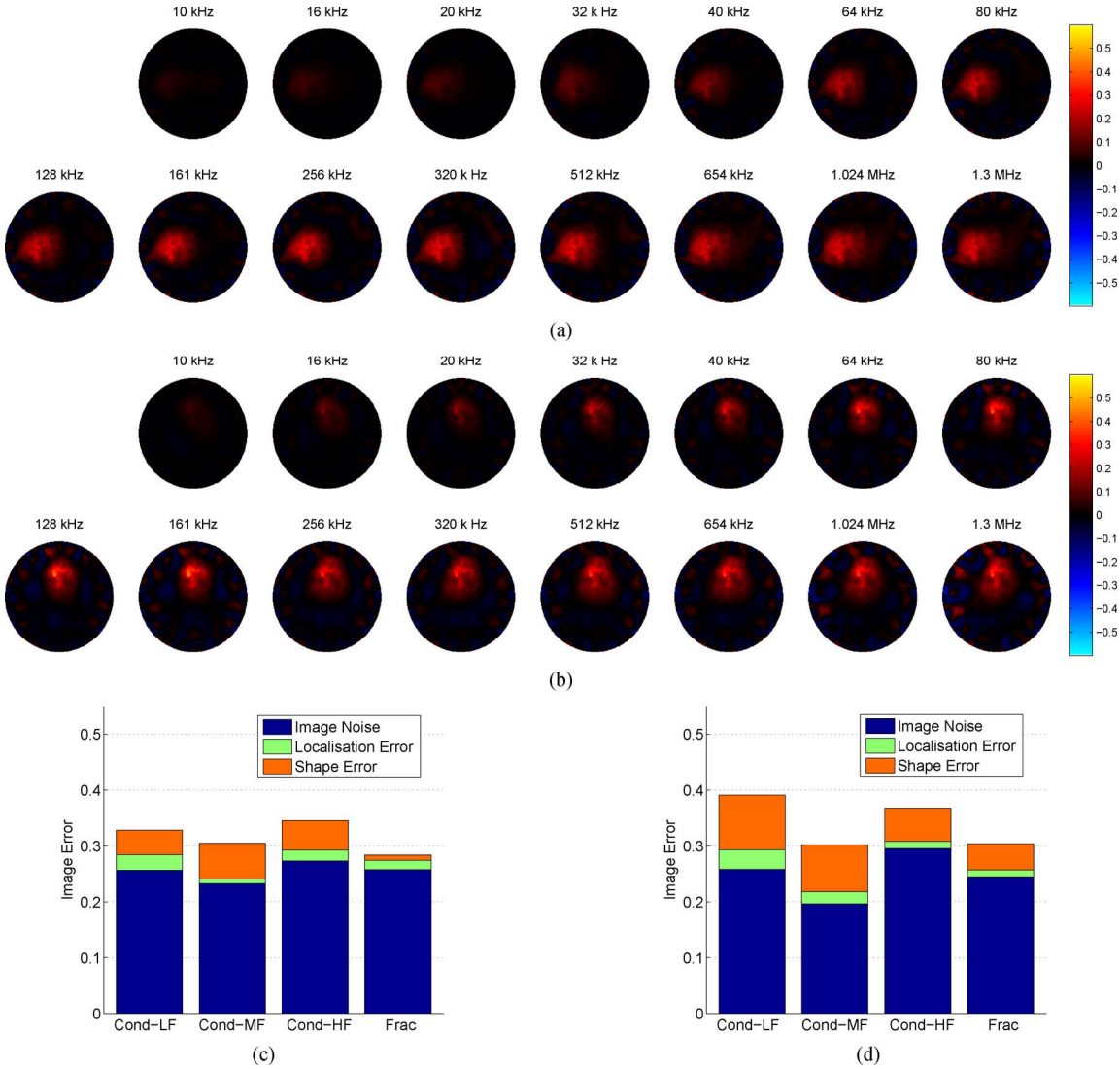

Fig. 7. Phantom WFD conductivity images for each measurement frequency: (a) position 1 and (b) position 2. Comparison of image quantification results for WFD conductivity images at 640 Hz (Cond-LF), 128 kHz (Cond-MF), and 1.2 MHz (Cond-HF), and fraction image (Frac): (c) position 1 and (d) position 2.

Fraction and WFD conductivity images were reconstructed [Fig. 8(c)–(e)]. The results show that our fraction method can produce significantly better images than WFD in the case that the assumptions of WFD are violated.

H. Multiple Tissue Case

The fraction reconstruction method was applied to a numerical phantom with four tissues. The same mesh, electrode positions, measurement protocol and frequencies were used as in the previous cases. The background was set to the conductivity values of saline-carrot sampled previously. The conductivity values of the potato sample were used to simulate a cylindrical perturbation of radius 2.2 cm and length 10 cm in position (0.87 cm 4.92 cm 0 cm). The conductivities of banana and cucumber samples were measured with an impedance analyzer using the method and instrumentation described in Section III-A [Fig. 9(a)]. These values were used to simulate two further perturbations of the same size in (-4.7 cm -1.71 cm 0 cm) (banana) and (3.83 cm -3.21 cm 0 cm) (cucumber). The boundary voltages were computed, and 0.1% proportional white noise was added to the absolute values. Fraction images were reconstructed for each tissue [Fig. 9(c)] using the proposed method. The regularization parameter was chosen by visual inspection, and the number of iterations was set to 10. The algorithm was successful in differentiating between the tissues, and returning high constrast. The L^2-norm error of the solution, defined by (20), is $\mathrm{Err}_{L^2} = 2.16\%$, which is approximately double the error found in the 2 tissue case (Fig. 3 and Section III-C).

I. Approximation Error Evaluation

A simulation study was performed to investigate the approximation introduced by the fraction model in representing the conductivity of an object. A sphere was simulated using a fine tetrahedral mesh of diameter 10 cm with 130,144 tetrahedral elements [Fig. 10(a)]. A conductivity distribution $\boldsymbol{\sigma}^f$ was drawn from the binomial distribution $\mathrm{p}(\boldsymbol{\sigma}^f) \sim \mathrm{B}(\epsilon_1, \epsilon_2)$, where $\epsilon_1 = 0.11$ and $\epsilon_2 = 0.05$ are approximately the conductivities of saline–carrot mixture and potato at 10 kHz.

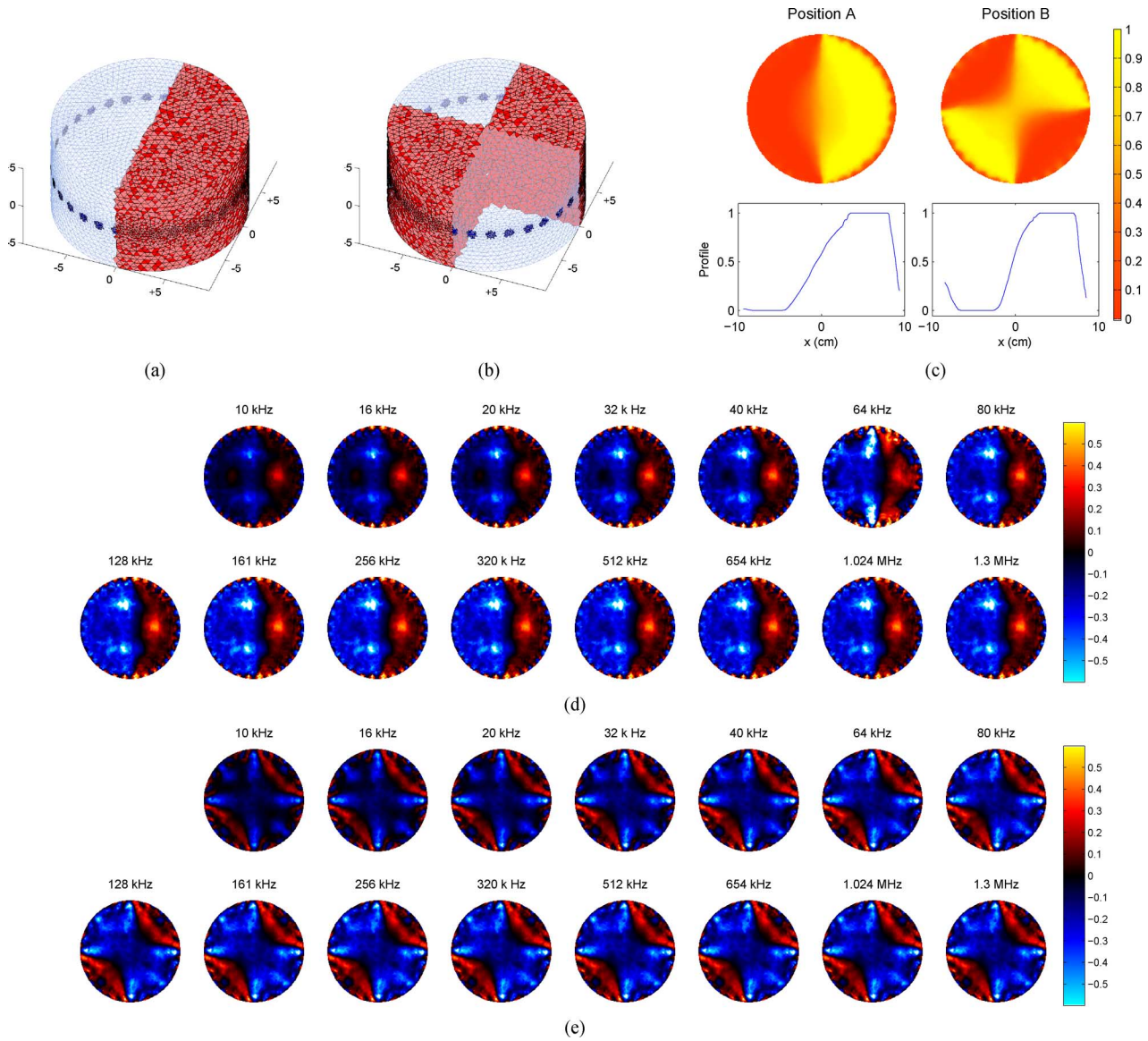

Fig. 8. Simulation model, and fraction and WFD conductivity images: (a) model of position A, (b) model of position B, (c) perturbation fraction images of position A and B, (d) WFD conductivity image of position A, (e) WFD conductivity image of position B.

A conforming mesh with 16 268 ($= 130,144/8$) elements [Fig. 10(b)] was used to define a second conductivity distribution $\boldsymbol{\sigma}^c$. The two meshes were chosen so that each tetrahedra of the coarse mesh would contain eight tetrahedra of the fine mesh, and each surface triangle of the coarse mesh would contain four triangles of the fine mesh. The conductivity of each element of the coarse mesh was obtained via linear combination of the corresponding elements of the fine mesh using the fraction model. Finally, the values $\boldsymbol{\sigma}^c$ were distributed on the fine mesh to generate a third conductivity distribution $\boldsymbol{\sigma}^{f^*}$.

The boundary conditions were set by simulating two electrodes in polar position. The electrode shape was chosen in order to maintain the same electrode area in the coarse and fine mesh. The radius of the circle circumscribing each electrode was 1 cm. We generated a current of peak amplitude $+133$ μA one electrode, and the other was used as ground. The electrode contact impedance was set at 1 kΩ and the complete electrode model was employed.

The boundary voltages v^c, v^f were generated, and v^{f^*} was obtained from the conductivity distributions defined above. The total modelling error $\mathrm{Err}_{\mathrm{total}} = \left|v^f - v^c\right|$ between the representations of $\boldsymbol{\sigma}^f$ and $\boldsymbol{\sigma}^c$, and the discretization error $\mathrm{Err}_{\mathrm{discr}} = \left|v^{f^*} - v^c\right|$ between the representations of $\boldsymbol{\sigma}^{f^*}$ and $\boldsymbol{\sigma}^c$ were considered. In order to evaluate the error introduced by the fraction model in estimating v_c, the percentile difference between the total and discretization error was considered

$$\mathrm{Err}_{\mathrm{frac}} = \frac{\mathrm{Err}_{\mathrm{total}} - \mathrm{Err}_{\mathrm{discr}}}{v^c} \cdot 100. \tag{22}$$

The random distribution $\boldsymbol{\sigma}^f$ was drawn and the fraction error was calculated 100 times. The procedure was repeated after reducing the proportion of mixed elements in the coarse mesh from 100% to 50% and 10% [Fig. 10(c)]. In order to achieve this, the values of the correct proportion of elements of the fine mesh were assigned at random and the remaining were consid-

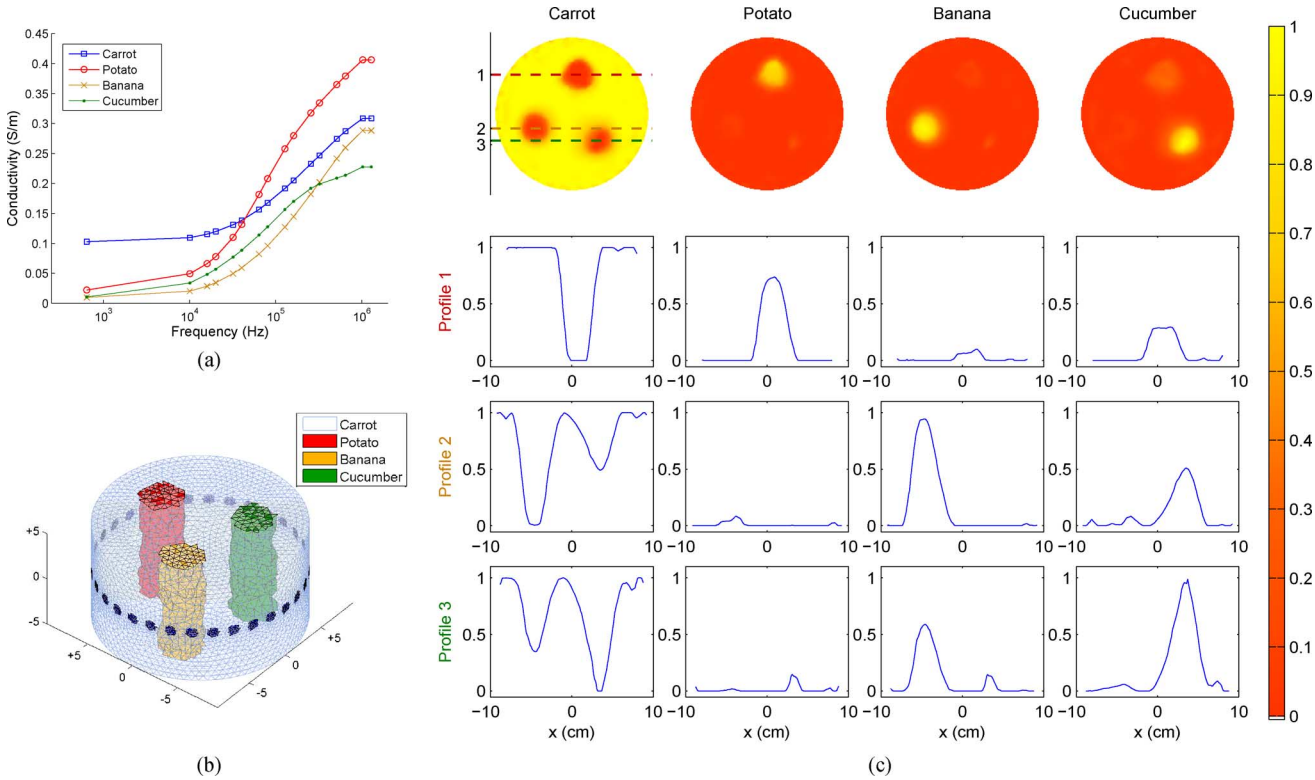

Fig. 9. Four-tissue case model and reconstruction: (a) conductivity values of carrot-saline, potato, banana and cucumber obtained from sample measurements, (b) numerical phantom model, scale is cm (c) reconstructed fraction images and profile plots at $y = +4.92$ cm (1), $y = -1.71$ cm (2), and $y = -3.21$ cm (3).

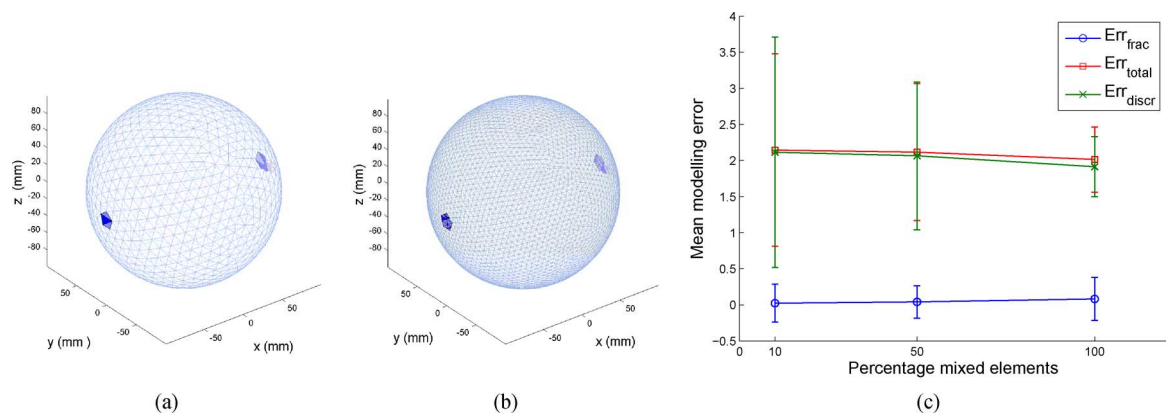

Fig. 10. Approximation error evaluation model and results: (a) coarse mesh, 16 268 elements; (b) fine mesh, 130 144 elements; (c) mean approximation error introduced by the fraction model ($\mathrm{Err}_{\mathrm{frac}}$), the FEM ($\mathrm{Err}_{\mathrm{discr}}$) and both methods ($\mathrm{Err}_{\mathrm{total}}$) in estimating boundary voltages for 10%, 50%, and 100% mixed elements in a coarse mesh.

ered in homogeneous groups of 8, each corresponding to an element of the coarse mesh.

In this example the approximation error given by the fraction model is significantly smaller than that introduced by the coarsening of the mesh. Furthermore, the error is present only in the representation of mixed elements and thus depends on the proportion of mixed-to-homogeneous elements. If tissues occupy a distinct area of the image and mixed elements are limited to those lying across the boundaries, the approximation error is small. If a large area is occupied by a mixture of tissues, the approximation error can be reduced by modelling the mixture rather than the individual tissues.

IV. Conclusion

We have formalized, validated and applied a nonlinear fraction reconstruction method for performing multifrequency EIT using spectral constraints. We have investigated the robustness of our method to errors in the assumed spectra and found that, in the case examined, the method is resistant to a small amount of uncertainty. We have shown, using phantom data, that the proposed method can result in improved image quality when compared to absolute and weighted frequency-difference conductivity imaging. The direct use of multifrequency data has proved more robust than fitting multifrequency conductivity

images. We have shown using simulated data that the proposed method is superior to weighted frequency-difference imaging when the assumptions of the latter are violated. We have applied our method to a numerical phantom with four tissues and shown that it is possible to distinguish between multiple tissues and accurately reconstruct the fraction image of each one. These results suggest that fraction imaging may be suitable for producing one-off clinical diagnostic images using EIT.

The advantages of using spectral constraints in multifrequency EIT are twofold. First, the choice to reconstruct the fraction values, which are frequency independent, allows for the direct and simultaneous use of all multifrequency data. The dimensionality of the problem depends on the number of elements and tissues, and not on the number of frequencies. Therefore it is preferable to use data acquired at all measurement frequencies. As long as the number of frequencies is larger than the number of tissues, implementation of the fraction method increases the number of constraints in the reconstruction and results in a reduction in the degrees of freedom of the problem. Secondly, knowledge of the tissue spectra allows for the use of difference data in the objective function, thus resulting in the subtraction of modelling and frequency independent instrumentation errors in a nonlinear reconstruction scheme. In conductivity imaging this is not possible because it would require simultaneous estimation of the measurement and reference conductivities, thus increasing the degrees of freedom of the problem. The fraction images could be improved by modelling the change in contact impedance over frequencies. This would result in a further reduction of the edge artefact.

The fraction reconstruction method requires prior knowledge of the tissues' impedance spectra. These can be readily obtained from the literature, or estimated empirically. Accurate modelling of biological tissues is crucial for clinical applications. The number T of tissue types could be inferred by iteratively applying the algorithm with increasing values of T until a criterion is reached (e.g., no sharp increase in model likelihood). It would be preferable to model all possible or expected distinct tissues, so that if t is the actual number of tissues, $T \geq t$. The reconstructed fraction values of the tissues that are not present would then be zero. However, a reduction in image quality is to be expected if $T \gg t$. We aim in future studies to relax the assumptions of the fraction model and allow for variability and heterogeneity in the tissue spectra. This could be achieved by using statistical methods to infer subject-specific deviations in the spectral properties of the tissues from the boundary voltage data, under certain constraints. Further studies are necessary to determine how image quality varies with the number of tissues and frequencies.

REFERENCES

[1] B. H. Brown, A. D. Leathard, L. Lu, W. Wang, and A. Hampshire, "Measured and expected Cole parameters from electrical impedance tomographic spectroscopy images of the human thorax," *Physiolog. Meas.*, vol. 16, no. 3A, pp. A57–67, Aug. 1995.

[2] A. R. Hampshire, R. H. Smallwood, B. H. Brown, and R. A. Primhak, "Multifrequency and parametric EIT images of neonatal lungs," *Physiolog. Meas.*, vol. 16, no. 3A, pp. A175–89, Aug. 1995.

[3] A. Romsauerova, A. McEwan, L. Horesh, R. Yerworth, R. Bayford, and D. Holder, "Multi-frequency electrical impedance tomography (EIT) of the adult human head: Initial findings in brain tumours, arteriovenous malformations and chronic stroke, development of an analysis method and calibration," *Physiolog. Meas.*, vol. 27, no. 5, pp. S147–61, May 2006.

[4] V. Kolehmainen, M. Vauhkonen, P. Karjalainen, and J. Kaipio, "Assessment of errors in static electrical impedance tomography with adjacent and trigonometric current patterns," *Physiolog. Meas.*, vol. 18, no. 4, p. 289, 1997.

[5] A. McEwan, G. Cusick, and D. S. Holder, "A review of errors in multi-frequency EIT instrumentation," *Physiolog. Meas.*, vol. 28, no. 7, pp. S197–215, Jul. 2007.

[6] B. Packham, H. Koo, A. Romsauerova, S. Ahn, A. McEwan, S. C. Jun, and D. S. Holder, "Comparison of frequency difference reconstruction algorithms for the detection of acute stroke using EIT in a realistic head-shaped tank," *Physiolog. Meas.*, vol. 33, no. 5, pp. 767–786, May 2012.

[7] J. K. Seo, J. Lee, S. W. Kim, H. Zribi, and E. J. Woo, "Frequency-difference electrical impedance tomography (fdEIT): Algorithm development and feasibility study," *Physiolog. Meas.*, vol. 29, no. 8, pp. 929–44, Aug. 2008.

[8] S. C. Jun, J. Kuen, J. Lee, E. J. Woo, D. Holder, and J. K. Seo, "Frequency-difference electrical impedance tomography (fdEIT): Validation by simulation and tank experiment," *Physiolog. Meas.*, vol. 30, no. 10, pp. 1087–99, Oct. 2009.

[9] S. Ahn, T. I. Oh, S. C. Jun, J. K. Seo, and E. J. Woo, "Validation of weighted frequency-difference EIT using a three-dimensional hemisphere model and phantom," *Physiolog. Meas.*, vol. 32, no. 10, pp. 1663–80, Oct. 2011.

[10] R. J. Yerworth, L. Horesh, R. H. Bayford, A. Tizzard, and D. S. Holder, "Robustness of linear and non-linear reconstructions algorithms for brain EITS," in *IFMBE Proc.*, Gdansk, Poland, 2004, vol. 44, pp. 499–502.

[11] L. Horesh, R. H. Bayford, R. J. Yerworth, A. Tizzard, G. M. Ahadzi, and D. S. Holder, "Beyond the linear domain-The way forward in MFEIT image reconstruction of the human head," in *IFMBE Proc.*, Gdańsk, Poland, 2004, vol. 3, pp. 683–686.

[12] A. Corlu, R. Choe, T. Durduran, K. Lee, M. Schweiger, S. Arridge, E. M. C. Hillman, and A. G. Yodh, "Diffuse optical tomography with spectral constraints and wavelength optimization," *Appl. Opt.*, vol. 44, no. 11, pp. 2082–93, Apr. 2005.

[13] A. McEwan, A. Romsauerova, R. Yerworth, L. Horesh, R. Bayford, and D. S. Holder, "Design and calibration of a compact multi-frequency EIT system for acute stroke imaging," *Physiolog. Meas.*, vol. 27, no. 5, pp. S199–210, May 2006.

[14] J. Nocedal and S. Wright, *Numerical Optimization*. New York: Springer-Verlag, 1999, Springer Ser. Operat. Res. Finan. Eng..

[15] Y. Saad and M. H. Schultz, "GMRES: A generalized minimal residual algorithm for solving nonsymmetric linear systems," *SIAM J. Sci. Stat. Comput.*, vol. 7, no. 3, pp. 856–869, 1986.

[16] R. P. Brent, *Algorithms for Minimization without Derivatives*. Englewood Cliffs, NJ: Prentice-Hall, 1973.

[17] E. Ziegel, W. Press, B. Flannery, S. Teukolsky, and W. Vetterling, "Numerical recipes: The art of scientific computing," *Technometrics*, vol. 29, no. 4, pp. 164–168, Nov. 1987.

[18] L. Horesh, M. Schweiger, S. Arridge, and D. Holder, "Large-scale non-linear 3-D reconstruction algorithms for electrical impedance tomography of the human head," in *IFMBE Proc.*, 2007, vol. 14, pp. 3862–3865.

[19] L. Fabrizi, A. McEwan, T. Oh, E. J. Woo, and D. S. Holder, "An electrode addressing protocol for imaging brain function with electrical impedance tomography using a 16-channel semi-parallel system," *Physiolog. Meas.*, vol. 30, no. 6, pp. S85–101, Jun. 2009.

[20] E. Somersalo, M. Cheney, and D. Isaacson, "Existence and uniqueness for electrode models for electric current computed tomography," *SIAM J. Appl. Math.*, vol. 52, no. 4, pp. 1023–1040, 1992.

[21] C. Hansen and D. P. O'Leary, "The use of the L-curve in the regularization of discrete ill-posed problems," *SIAM J. Sci. Comput.*, vol. 14, no. 6, pp. 1487–1503, 1993.

[22] P. Hansen, T. Sekii, and H. Shibahashi, "The modified truncated SVD method for regularization in general form," *SIAM J. Sci. Stat. Comput.*, vol. 13, no. 5, pp. 1142–1150, 1992.